

LOFAR Observations of Substructure Within a Traveling Ionospheric Disturbance at Mid-Latitude

Gareth Dorrian¹ , Richard Fallows², Alan Wood¹, David R. Themens¹ , Ben Boyde¹, Andrzej Krankowski³, Mario Bisi² , Bartosz Dąbrowski³ , and Christian Vocks⁴ 

¹Space Environment and Radio Engineering Group (SERENE), University of Birmingham, Birmingham, UK, ²RAL Space, United Kingdom Research and Innovation, Science & Technology Facilities Council, Rutherford Appleton Laboratory, Harwell Campus, Oxfordshire, UK, ³Space Radio-Diagnostics Research Center, University of Warmia and Mazury in Olsztyn, Olsztyn, Poland, ⁴Leibniz-Institut für Astrophysik Potsdam (AIP), Potsdam, Germany

Key Points:

- A slow moving traveling ionospheric disturbance was detected exhibiting substantial internal substructure on scales of ~20 km
- The propagation of the traveling ionospheric disturbance was estimated by several methods to be ~65 ms⁻¹ in a North Westerly direction
- Substructure detected within the traveling ionospheric disturbance was larger than the Fresnel scale for the observation geometries and generated refractive scattering

Supporting Information:

Supporting Information may be found in the online version of this article.

Correspondence to:

G. Dorrian,
g.dorrian@bham.ac.uk

Citation:

Dorrian, G., Fallows, R., Wood, A., Themens, D. R., Boyde, B., Krankowski, A., et al. (2023). LOFAR observations of substructure within a traveling ionospheric disturbance at mid-latitude. *Space Weather*, 21, e2022SW003198. <https://doi.org/10.1029/2022SW003198>

Received 17 JUN 2022

Accepted 3 JAN 2023

Abstract The large scale morphology and finer sub-structure within a slowly propagating traveling ionospheric disturbance (TID) are studied using wide band trans-ionospheric radio observations with the LOw Frequency ARray (LOFAR; van Haarlem et al., 2013, <https://doi.org/10.1051/0004-6361/201220873>). The observations were made under geomagnetically quiet conditions, between 0400 and 0800 on 7 January 2019, over the UK. In combination with ionograms and Global Navigation Satellite System Total Electron Content anomaly data we estimate the TID velocity to ~60 ms⁻¹, in a North-westerly direction. Clearly defined substructures with oscillation periods of ~300 s were identified within the TID, corresponding to scale sizes of 20 km. At the geometries and observing wavelengths involved, the Fresnel scale is between 3 and 4 km, hence these substructures contribute significant refractive scattering to the received LOFAR signal. The refractive scattering is strongly coherent across the LOFAR bandwidth used here (25–64 MHz). The size of these structures distinguishes them from previously identified ionospheric scintillation with LOFAR in Fallows et al. (2020), <https://doi.org/10.1051/swsc/2020010>, where the scale sizes of the plasma structure varied from ~500 m to 5 km.

Plain Language Summary Radio waves traveling from distant cosmic radio sources undergo distortions as they transit the Earth's ionosphere. The distortions, usually referred to as ionospheric scintillation, permit the remote characterization of ionospheric behavior. In this study we use this phenomena to extract information about the presence of a traveling ionospheric disturbance (TID), including observing substructure within the TID of sizes ~20 km. The effect is to create sequences of radio signal focusing and enhancement followed by signal fading in observations of this radio scintillation using the LOw Frequency ARray telescope.

1. Introduction

The signal received at a ground-based radio antenna from a distant natural radio source is a convolution of the source and a time- and frequency-dependent variability in amplitude and phase induced by scattering from plasma irregularities in the ionosphere. These effects can be broadly divided into diffractive scintillation (Carrano et al., 2011; Singleton, 1970) and refractive scattering (e.g., Forte, 2008), and chiefly depend on the scale sizes of the plasma irregularities and the wavelength of the radio waves received (Booker, 1981; Booker & Majidihi, 1981). Observing the various manifestations of these signal variations therefore permits remote characterization of ionospheric behavior. When examining such variations in the high frequency (HF) to very high frequency (VHF) band, with corresponding radio wavelengths ranging between ~100 and 1 m, one can observe a wide variety of ionospheric scattering characteristics that span the refractive and diffractive domains (e.g., Fallows et al., 2014, 2020).

Ionospheric scintillation is the rapid variation (~1-s) in received amplitude and phase of radio waves transiting the ionosphere, due to diffractive scattering of the radio waves by small-scale plasma density features in the raypath (e.g., Tsunoda, 1985; Wild & Roberts, 1956; Yeh & Liu, 1982). Such plasma density features are highly structured (Bowman, 1981; Muralikrishna et al., 2007; Tsunoda, 1988) and rapidly alter the refractive index of the medium as a function of time and space, giving rise to the scintillations observed.

More specifically, the scintillation pattern is generated by many instances of constructive and destructive interference which occur between wavelets as they travel from the ionospheric scattering region to the observer. As

© 2023. The Authors.

This is an open access article under the terms of the [Creative Commons Attribution License](https://creativecommons.org/licenses/by/4.0/), which permits use, distribution and reproduction in any medium, provided the original work is properly cited.

the scattering region consists of many scatterers of different scale sizes which are moving across the raypath, some portion of the total power of the incoming radio wave will become reconfigured into a drifting scintillation pattern once it has crossed the space between the ionosphere and the observer and some will not. The scintillation pattern received by the observer is therefore a function both of ionospheric plasma scale size and distance between the observer and the ionosphere. The upper limit on scale size of the plasma scatterers which permit a fully developed scintillation pattern is called the Fresnel scale, or Fresnel limit, which is given by

$$F_D = \sqrt{2\lambda L} \quad (1)$$

where λ is the observed wavelength of the radio signal, and L is the distance from the observer to the ionospheric scattering region. As the population of plasma scatterers is in motion with respect to the observer the Fresnel scale can be converted to a Fresnel frequency, f_F , by

$$f_F = \frac{v_p}{F_D} \quad (2)$$

where v_p is the plane-of-sky propagation velocity of the scattering plasma as seen by the observer. Plasma structure scale sizes in the diffractive regime range from the Fresnel scale to approximately an order of magnitude below this value (Basu et al., 1998). For a given distribution of plasma scale sizes in the ionosphere, scintillation is more noticeable at HF and VHF (Groves et al., 1997). This is because lower frequencies correspond to larger Fresnel scale sizes, and hence the diffractive regime at larger Fresnel scales encompasses a greater proportion of the plasma scattering population.

Ionospheric scintillation is common at equatorial (e.g., Abdu et al., 1985) and auroral latitudes (e.g., Kinrade et al., 2012), but can be encountered at any location (Fremouw & Bates, 1971). It affects the accuracy of Global Navigation Satellite Systems (GNSSs) (e.g., Kintner et al., 2007; Prikryl et al., 2015) which operate in the UHF range, and imposes some limitations on synthetic aperture radio astronomy observations (Hinder & Ryle, 1971). Thorough reviews of ionospheric scintillation and the underlying physical mechanisms are given by Aarons (1982) and Priyadarshi (2015), and a thorough review of ionospheric irregularities at all latitudes is given by Fejer and Kelley (1980).

Refraction through the ionosphere is caused by plasma irregularities which have scale sizes greater than the Fresnel scale. Under instances of sufficiently strong fluctuations in plasma density involving larger-scale plasma features, refractive scattering is the dominant source of variations observed in received signal power, and particularly signal phase (Booker & Majidiah, 1981). Scattering effects of the ionosphere in general therefore pose challenges for low-frequency radio astronomy, and numerous authors have covered the subject in detail, including Mangum and Wallace (2015) and de Gasperin et al. (2018).

Traveling ionospheric disturbances (TIDs) are wave-like perturbations which are the ionospheric manifestation of atmospheric gravity waves (Hines, 1960), which can travel for thousands of km. They are generally categorized as large-scale TIDs (LSTIDs), typically driven by auroral sub-storms (Cherniak & Zakharenkova, 2018; Hunsucker, 1982) and stochastic impulsive events such as volcanic eruptions (Themens et al., 2022). LSTIDs exhibit wavelengths of the order of 1,000 km, propagation velocities from 400 to 1,000 ms⁻¹, and periods typically of 30 min to several hours.

Shiokawa et al. (2003) conducted a statistical study of night-time medium-scale traveling ionospheric disturbances (MSTIDs) over Japan and found a preferential propagation direction to the South West, with velocities of between 50 and 100 ms⁻¹, and wavelengths of 100–300 km. Nishitani et al. (2019), also noted the preponderance of Westward propagating night-time MSTIDs with low velocities of ~10s ms⁻¹, as detected by SuperDARN (Greenwald et al., 1995).

Smaller scale traveling ionospheric disturbances (SSTIDs) are also a feature of the ionosphere although they are reported less often than LSTIDs and MSTIDs. Recently LOW Frequency ARray (LOFAR) has been used to detect SSTIDs and a model has been developed to investigate ionospheric scintillation of these features in detail by Boyde et al. (2022).

The very wide field-of-view, high time cadence, and large bandwidth (10–250 MHz) afforded by the LOFAR (van Haarlem et al., 2013) make it an ideal instrument with which to investigate ionospheric plasma structures over a

Table 1
Observation Summary and Approximate Event Timings From LOw Frequency ARray Observations of Cassiopeia A and Cygnus A on 7 January 2019

Observation	Cassiopeia A elevation	Cassiopeia A Azimuth	Cygnus A elevation	Cygnus A Azimuth	Notes
UK608LBA					
0400	20.2°	356.7°	9.9°	32.9°	Observation Start
0519	20.6°	8.3°	Event not seen	Event not seen	Event onset, Cass. A
0554	21.6°	12.3°	Event not seen	Event not seen	Event end, Cass. A
0800	28.4°	28.3°	39.1°	70.6°	Observation End
IE613 LBA					
0400	22.5°	353°	9.6°	28.5°	Observation Start
0552			19.9°	47.7°	Event onset, Cyg. A
0632	23.9°	14.1°			Event onset, Cass. A
0646			26.4°	56.4°	Event end, Cyg. A
0721	26.1°	20.6°			Event end, Cass. A
0800	25.6°	28.4°	36.1°	67.9°	Observation End

range of frequencies. Many previous studies have tended to utilize one frequency or a small range of frequencies (e.g., Groves et al., 1997; Mitchell et al., 2005; RamaRao et al., 2006; Song et al., 2022) from GNSS or other systems. However, the scattering effect of ionospheric structures can be seen across wide bandwidths, particularly when observing natural radio sources (e.g., Fallows et al., 2014). In this paper we describe the observations of a rapidly evolving ionospheric transient feature during a LOFAR observation of the natural radio sources Cygnus A (3C405), and Cassiopeia A (3C461), on 7 January 2019. Natural radio sources lend themselves well to ionospheric scintillation studies of this kind as they are inherently broadband emitters and thus permit observations of ionospheric influences on transited radio signals over a wide bandwidth. Cassiopeia A and Cygnus A are also two of the strongest natural radio source in the sky located outside the solar system.

Each LOFAR station consists of two arrays, a Low-Band Antenna (LBA) array of dual-polarisation crossed dipole antennas suspended above the ground plane, and which cover the frequency range 10–90 MHz and a High-Band Antenna array of tiles, each tile consisting of a phased array of 16 dual-polarisation bow tie antennas, which covers the range 110–270 MHz. In this paper, we use data from the LBAs at the Irish and UK LOFAR stations (Station codes IE613 and UK608 respectively). IE613 is located near Birr in central Ireland at 53.10°N, 7.92°W; UK608 is located near Chilbolton in the South of England at 51.14°N, 1.43°W. Supporting Information from the Fairford ionosonde (FF051: 51.71°N, 1.79°E) from the Global Ionospheric Radio Observatory (Reinisch & Galkin, 2011) underlying the feature and GNSS Total Electron Content (TEC) data from the British Isles continuous GNSS Facility are also used. The GNSS TEC in particular provide a useful global context for the large-scale morphology of the feature. LOFAR provides excellent high time resolution observations of the sub-structure within the feature, and the ionosondes enable the altitude of the feature to be approximated. Geophysical indices and data from suitably located ground-based magnetometers are also used to establish the overall space weather context at the time of these observations.

2. Observations

The data upon which this study was based were collected during LOFAR observations of 3C405 (Cygnus A: RA 19 hr 59 min 28 s and Declination 40.73°) and 3C461 (Cassiopeia A: RA 23 hr 23 min 24 s and Declination 58.82°) by IE613 and UK608, between 0400 and 0800 on 7 January 2019. All times quoted through this paper are in UT. These station locations are shown in Figure 8. The raw data for this observation can be obtained from the LOFAR long-term archive (<https://lta.lofar.eu>); observation ID L691956 under project LT10_006. From the perspective of both LOFAR stations, the radio sources were observed to rise in elevation and rotate clockwise in azimuth during the observing window (see Figure 8). A summary of the observing parameters is given in Table 1, showing the event onset and event end times for the two radio sources and the two LOFAR stations used. All times henceforth are given in.

Given that the observation took place over a 4-hr window, the significant changes in elevation and azimuth of both sources was reflected in a general increase in received intensity from the radio sources over all observing frequencies during the window. It was therefore necessary to remove the time-of-day dependence from the received signal power for the whole data set. This was achieved by dividing the data in each sub-band channel by a fitted third order polynomial. Removal of RFI noise spikes was achieved by median filtering of each channel in a sliding window of 50 data points, corresponding to ~ 0.5 -s, and finding the standard deviation. Data points exceeding a 5σ threshold within this window were removed.

The LOFAR frequency coverage used here extends over 200 evenly spaced sub-bands of 195.3125 kHz, from 24.99 to 63.86 MHz. Note that the minimum and maximum frequencies quoted are the mid-points of their respective channels. The extrema of the full LBA bandwidth are excluded as they are often contaminated with heavy RFI from HF signals trapped in the Earth-ionosphere waveguide at the low end and heavily filtered to exclude FM radio signals at the high end. Each channel is a one-dimensional time series of received intensity, averaged to a time resolution of 0.01s.

Figures 1 and 2 show the observation from the UK and Irish LOFAR stations respectively. RFI contamination still persists in a small number of channels and these are visible as horizontal streaks. In these plots the data have been averaged to 1-s across the full 4-hr observing window for both LOFAR stations and on both radio sources. The exact start and end times of the observation window are 04:00:00.0 to 07:59:59.5 respectively; the total number of timestamps at 1-s resolution is 14,455. In the top panel of Figure 1 it can be seen that the dynamic spectrum of Cygnus A from the UK station (hereafter UK-CygA) shows little obvious disturbances except near the very end of the observing window; the ionosphere along this raypath is relatively undisturbed. Dynamic spectra from other nearby LOFAR stations such as France (FR606: 47.4°N 2.2°E) also showed no significant activity during this time.

However, in the dynamic spectrum of Cassiopeia A (UK-CassA) from the same station, a distinct series of near-vertical signal fadings and enhancements can be seen beginning at 0519 which continued for approximately 29 mines, ending at 0554. At 0552 a very similar feature appears in the dynamic spectra of Cygnus A as seen from the Irish LOFAR station (Figure 2, top panel, hereafter Irl-CygA). It continues for approximately 54 mines, ending at 0646. Fainter but similar looking structures appear briefly at the very end of the observation. Beginning at 0632, in Cassiopeia A also on the Irish station (Figure 2, bottom panel; hereafter Irl-CassA), a series of signal enhancements, curving slightly to both earlier and later times at the lower frequencies, are seen shortly before a deep signal fade across all bandwidths which lasts for ~ 500 s. After signal power levels return there are a couple of fainter signal enhancements before the feature transits o of the raypath. The entire feature lasts some 49 min, ending at 0721. Figures 1 and 2 are arranged in order of time of event onset, with the event first being seen in UK-CassA, then Irl-CygA, then Irl-CassA.

In all cases where ionospheric features were observed, the ionosphere beforehand and afterward was undisturbed, enabling an unambiguous identification of the start and end times. The fact that the feature is not seen during the UK-CygA observations is interesting; nor was it seen in any of the other LOFAR stations taking part in the same observation. This will be discussed in the following section. Given that such high time resolution is available, some sections of the various features observed are shown in more detail in Figure 3.

With such closer examination, finer structures can be discerned within. At the lower frequencies some slight curvature in the vertical structures can be seen, particularly in Irl-CassA. Between the main vertical bright features in all dynamic spectra, fainter but similar vertical structures are visible within darker regions which, at lower resolution, might be regarded as signal fades, hinting at the cascade of turbulent scale sizes within the scattering plasma. In Irl-CygA some of the vertical features near the middle of the event can be seen to split into doublets in the higher frequency ranges of ~ 45 – 65 MHz.

3. Analysis

3.1. Geophysical Context

The Kp index at the start of the observations (0400) was 2+ and at the end (0800) had dropped slightly to 1+. Local K-indices from the observatories at Eskdalemuir (ESK; 55.3°N, 3.2°W) and Lerwick (LER; 60.2°N, 1.1°W) did not go above 1+ during the observation. The Dst index decreased slightly from -5 to -15 nT over

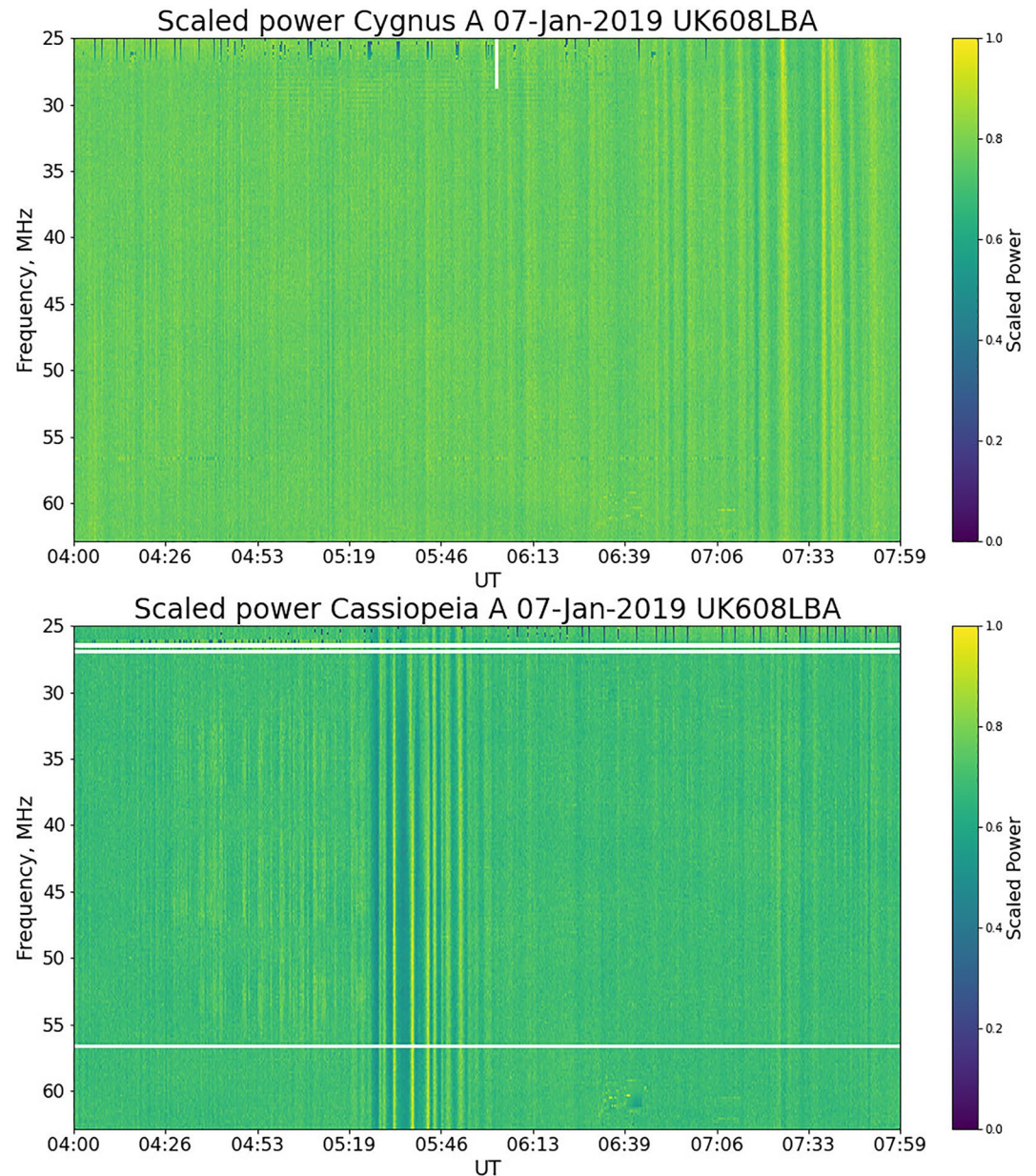


Figure 1. Dynamic spectra for the UK Low Frequency ARray station (UK608LBA) from 0400 to 0800 on 7 January 2019. The top panel shows the data collected from observations of Cygnus A and the bottom panel shows likewise from Cassiopeia A. The horizontal streaks are RFI. Event onset in Cassiopeia A is at 0520.

the course of the observing period. No solar radio bursts were recorded during the period of the event and the differences in event onset time at the different LOFAR stations demonstrate that these events were localized to the ionosphere rather than from emission sources in the solar wind. Figure 4 shows the SYM-H, ASY-H, and ASY-D indices from 0000 to 1200 on 7 January 2019; neither ASY-H nor ASY-D exceed ± 25 nT during this time period. Geomagnetic conditions at this time were therefore quiet.

3.2. GNSS TEC Anomalies and Ionosondes

To characterize the overall morphology and position of the feature seen in the LOFAR data and to further explain why the feature was not seen in UK-CygA, vertical TEC anomaly maps have been produced using data from ground based GNSS stations throughout the UK. The processing used to generate these maps is outlined in detail

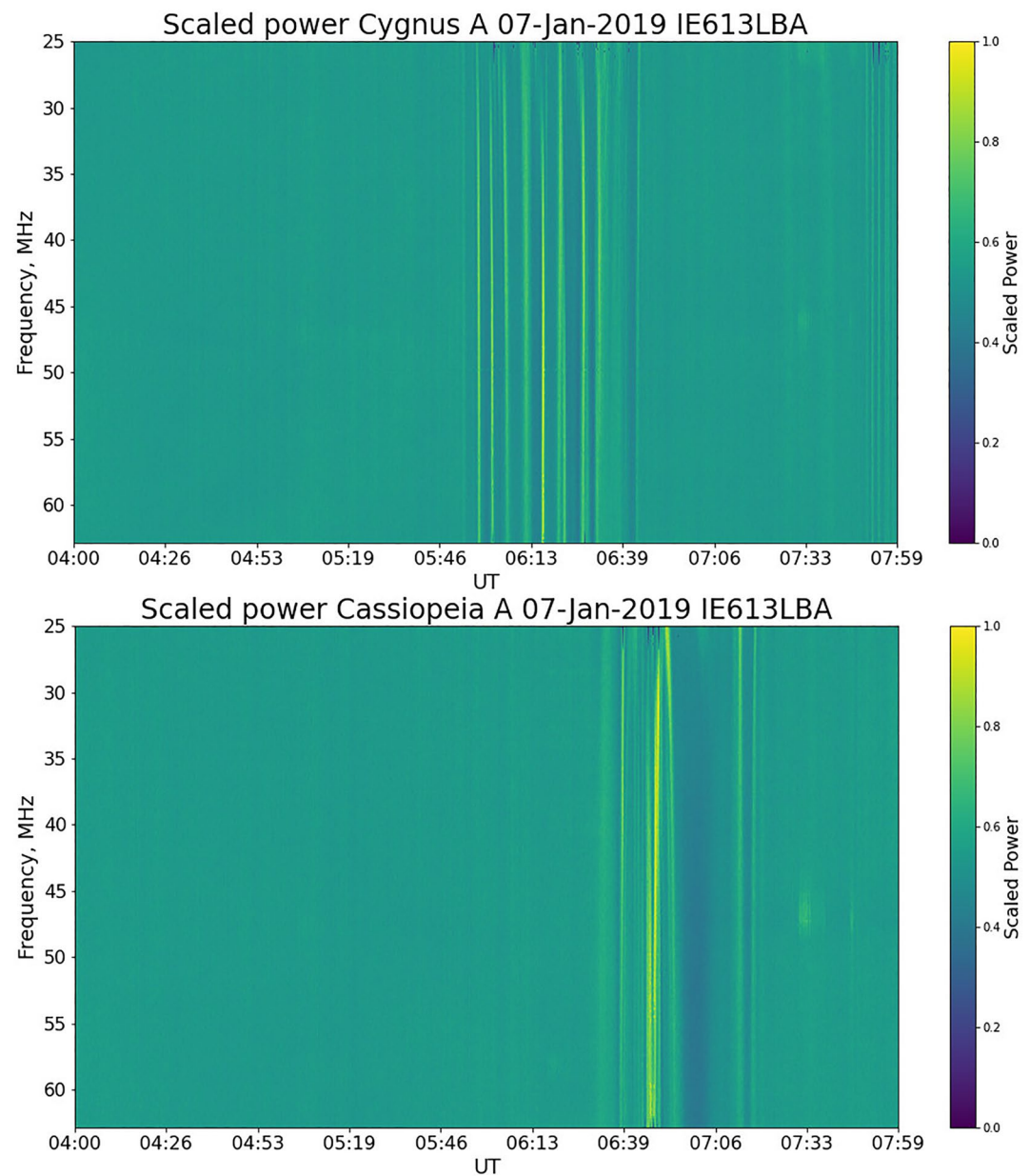


Figure 2. Dynamic spectra from the Irish LOw Frequency ARray station (IE613LBA) showing observations of Cygnus A (top panel) and Cassiopeia A (bottom panel).

in Themens et al. (2022). These maps, seen in Figure 5, show relative deviations in v TEC from a running 30-minute average. GNSS coverage is constrained to the land area of the UK; however, these maps use data from GNSS satellites at all elevations $>30^\circ$, enabling some coverage over the surrounding sea. Each pixel has a resolution of 0.5° in longitude and latitude. Ionospheric features are shown for an approximate altitude of 400 km. Yellow indicates a positive deviation in relative v TEC, blue shows a negative drop in relative v TEC.

A TID, comprised of at least two clear positive TEC anomaly wave peaks (in yellow) and interspersed with negative TEC anomaly troughs (in blue), is clearly resolved over Southern England and is seen to propagate slowly from Southeast to Northwest from 0500 to 0600 (Figure 5, left panels). The wavelengths of the TID are approximately 3° at the resolution of the maps, corresponding to a distance of approximately 300 km. Indicative of the slow propagation of the TID is the fact that it is not seen in versions of these maps using a 7-minute running average (not shown).

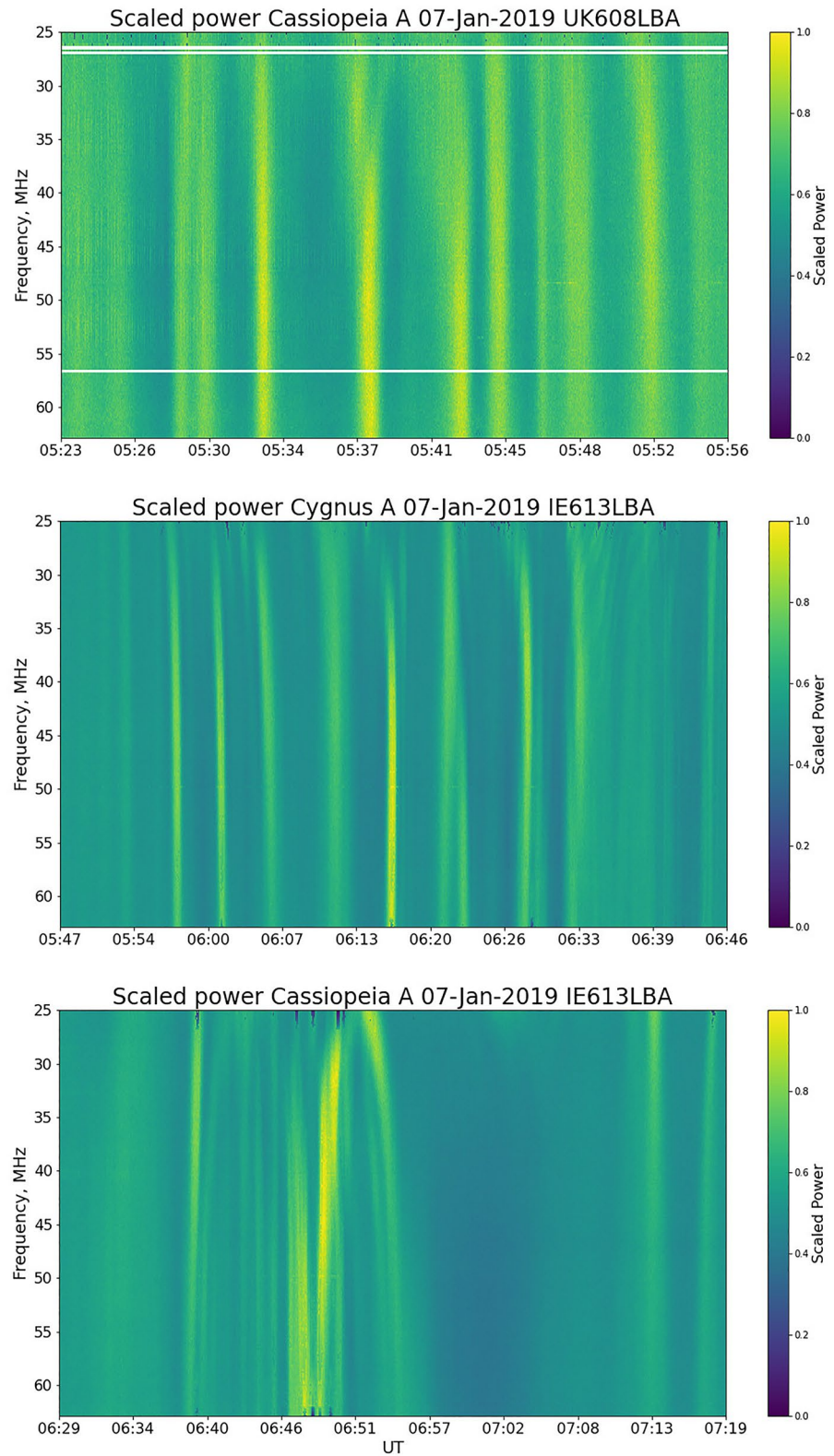


Figure 3. Close up views of all features of interest in UK-CassA, Irl-CygA, and Irl-CassA observations.

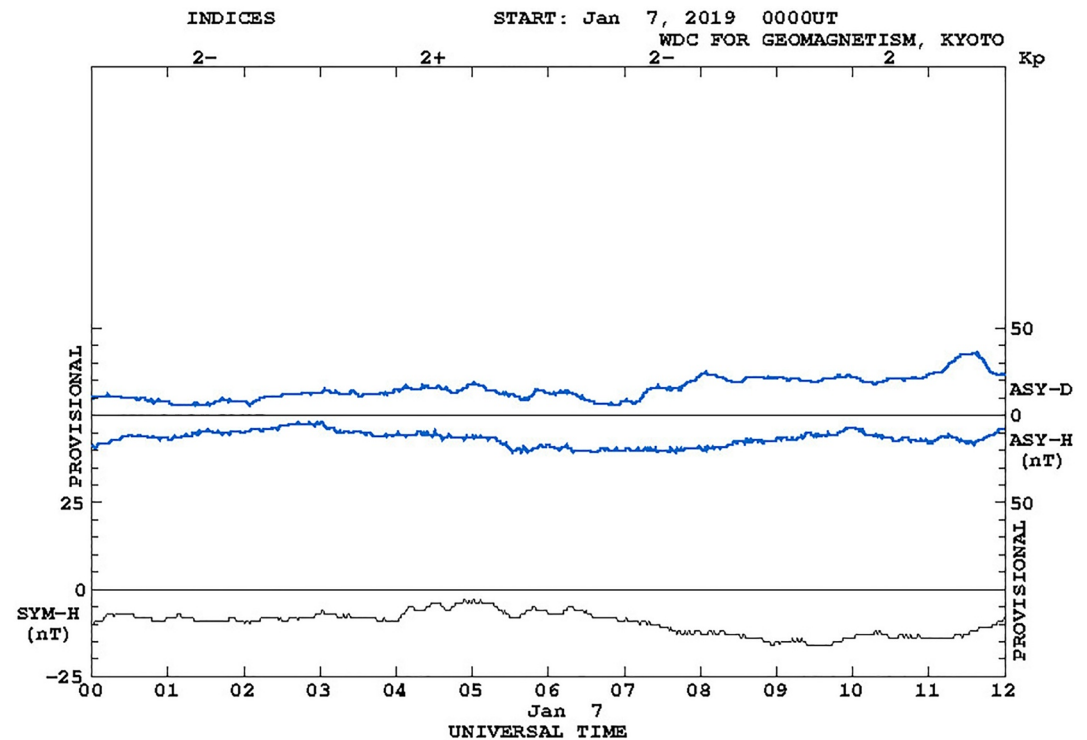


Figure 4. ASY-D, ASY-H, and SYM-H indices from 0000 to 1200 on 7 January 2019, showing quiet geomagnetic conditions.

The position of the Fairford ionosonde (red star, Figure 5) underlies the propagation of the TID. Ionosondes emit radio waves in a vertical cone above them which backscatter off ionospheric plasma and return to the receiver. Thus any population of moving plasma within the cone will induce a Doppler shift in the received backscatter which can be combined with angle of arrival information to infer the approach and recession of different plasma populations in different directions. It is important to note that the recession and approach of plasma populations revealed by a Doppler ionogram may also be due to a vertical velocity component. Doppler ionograms therefore provide a coarse overview of whether the bulk plasma flow above them is approaching, resulting in blue-shifted backscatter, or receding, resulting in red-shifted backscatter.

For the Fairford ionosonde, in addition to echo power and angle of arrival information, a coarse measurement of the echo Doppler is measured within the ionogram mode. This is generally used to help filter extraneous features from the ionograms. While this is very coarse and does not compare to purpose-built ionosonde drift modes, it can be used to at least infer whether structures are moving toward or away from the instrument. Alongside the TEC anomalies, Figure 5 also shows four time-coincident Doppler ionograms from the Fairford ionosonde, where only the O-mode echoes have been plotted.

Figure 6 shows the Doppler ionograms from FF051 at 15-minute timesteps from 0400 to 0545 and azimuth ionograms, for O-mode echoes, for the same times. This time window covered the transition of the TID as it passed overhead. Multiple colors in the azimuth plots reveal the presence of multiple populations of plasma in the transmission cone of the ionosonde at different azimuths.

In the first plot for example, at 0400, the light-red in the Doppler ionogram reveals a general recession of plasma at all frequencies, with the exception of a small population of blueshifted echoes at ~ 2 MHz. These lower frequency echoes correspond to a region of lower plasma density which clearly lies in the same position as the purple in the corresponding azimuthal ionogram showing that this lower plasma density population lies to the West (purple in the azimuthal plot).

Generally, from 0400 to 0500, the predominantly red points in the azimuthal ionograms across the full frequency space indicate the majority of echoes are from North of the ionosonde and are suggestive of a Northwards

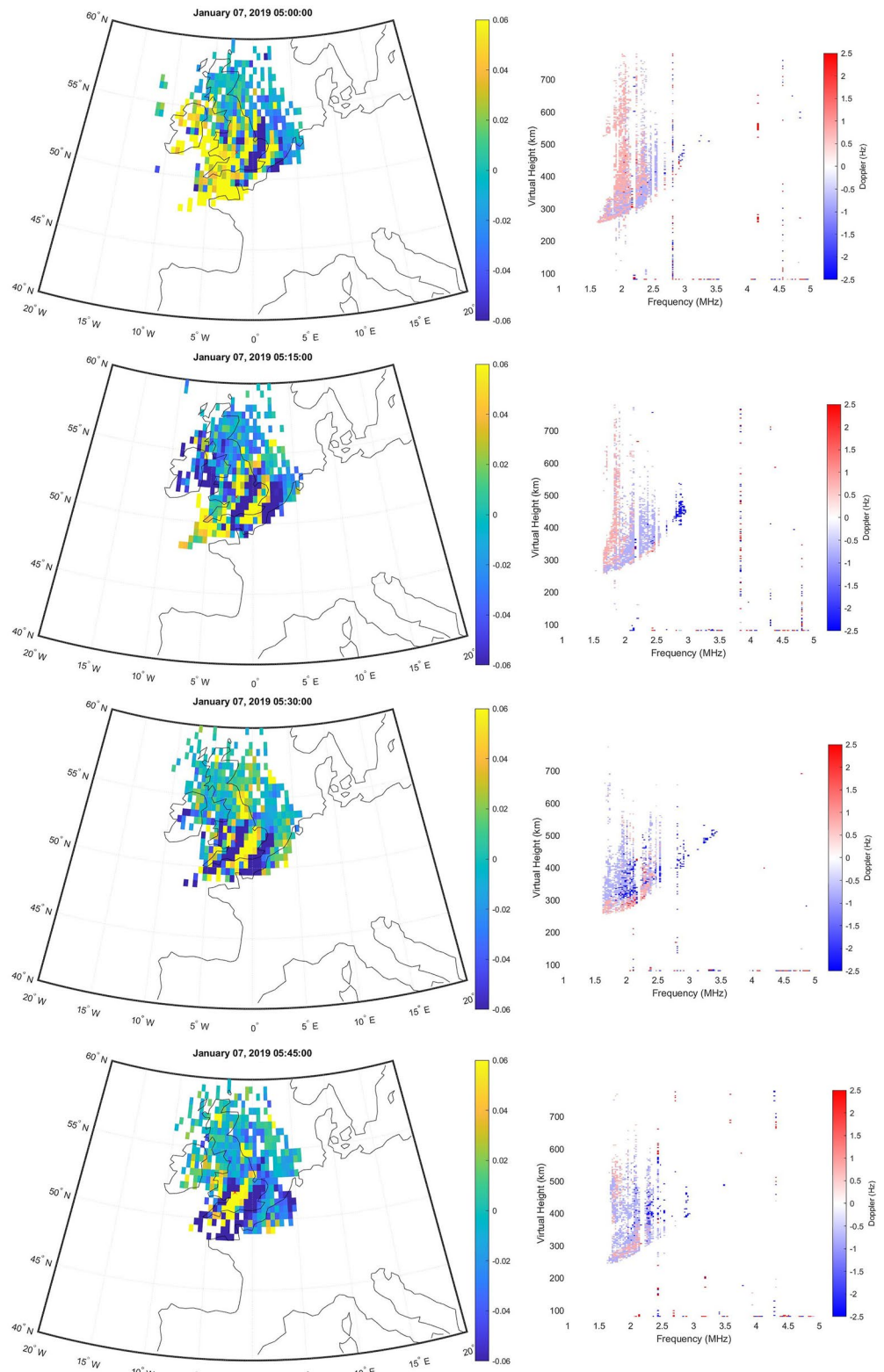


Figure 5. Global Navigation Satellite System (GNSS) Total Electron Content anomaly maps from 0500 to 0545 in 15-minute timesteps, using 30-minute averaged GNSS data and time coincident Doppler ionograms from the Fairford ionosonde (position indicated by red star).

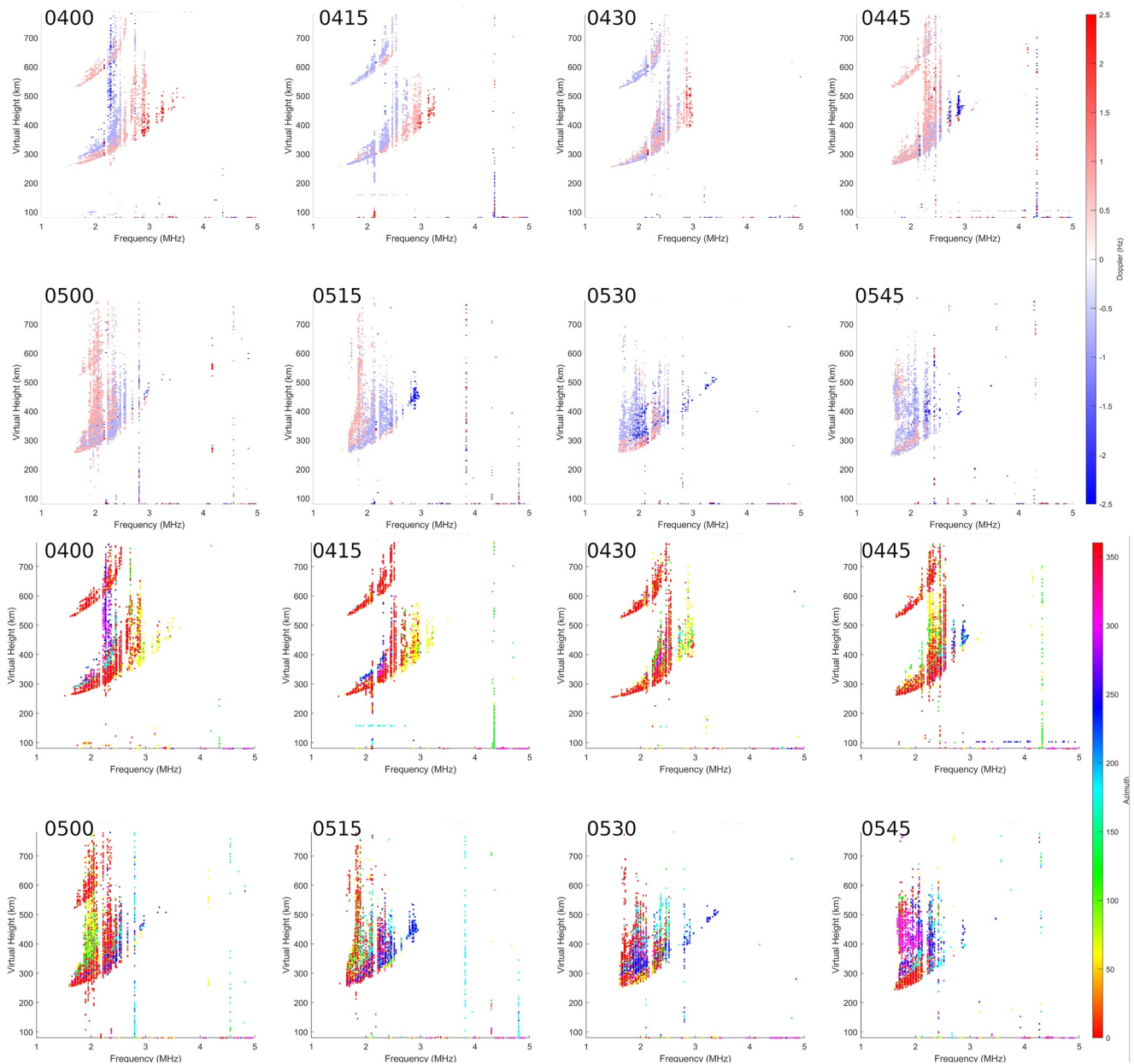


Figure 6. The upper eight panels show Doppler ionograms every 15-mines from 0400 to 0545 as the lead plasma enhancement of the traveling ionospheric disturbance passed over the Fairford ionosonde, followed by the approach of the plasma trough. Spread-F is also apparent throughout. The lower eight panels show azimuthal ionograms from the same times.

background plasma gradient overhead. The redshifted echoes corresponding to this Northwards background may also indicate a general vertical lifting of the ionosphere as the first of the peaks in the TID approaches. Smaller short lived populations of echoes at multiple frequencies and azimuths are also present throughout this period which may be caused by the passage of smaller scale ionospheric structures overhead.

At 0500 a clear population of green echoes appear at lower frequencies indicating the presence of an ionospheric density depletion to the South of the ionosonde. From 0515 onwards the colors become less coherent, with echoes coming from many directions and hence, many different plasma structures. This also coincides with Doppler ionograms which show a mixture of red and blue indicating that echoes are being received from some plasma that is approaching the ionosonde whilst other structures are receding. Taken together this shows rapid fluctuations in ionospheric plasma density gradient above the ionosonde as the highly structure peak in the TEC anomaly passes overhead.

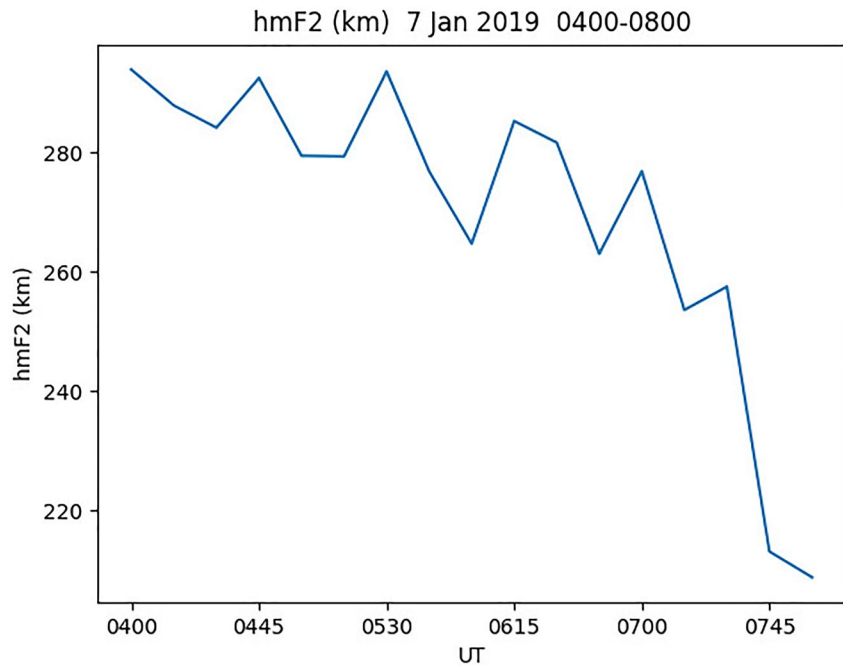


Figure 7. hmF2 from the Fairford ionosonde, 7 January 2019, 0400–0800.

From 0515 to 0545, significant populations of blueshifted plasma are seen in the Doppler plots, corresponding to azimuths the Northwest. This corresponded with the ionosonde lying beneath the trough of the TID; the peak was propagating away to the Northwest and as it moved out of the transmission cone the altitude of the bulk scattering plasma in the ionosphere descended, causing blueshifting. A decrease in hmF2 was also seen during this period, as can be seen in the hmF2 plot in Figure 7.

Moreover, the points on the later ionograms are more strongly clustered at lower plasma frequencies, which corresponds to a reduction in plasma density. These features are also consistent with the approach of the trough in the TID, between the first and second peaks. Clustering of the data points in all these ionograms is also consistent with spread-F and trace bifurcation, associated with TID presence in ionograms (Cervera & Harris, 2014; Moskaleva & Zaalov, 2013).

TIDs are compound structures which stretch over large height ranges, however these ionograms also enable a physical basis for the altitude of the TID to be estimated. As can be seen in Figure 7, the hmF2 altitude varied considerably over the course of the observing time between a maximum of 293 km and a minimum of 208 km, averaging at 270 km. This altitude was therefore used to constrain the LOFAR observing geometry shown in Section 3.3.

3.3. LOFAR Observing Geometry

Using the geometry outlined in Figure 1 of Birch et al. (2002), the angle subtended at the center of the Earth (ψ) between a line to the LOFAR station at ground level, of length R_E (radius of Earth), and another line extending to the ionospheric pierce point (IPP) of length $R_E + h$, where h is the vertical height above ground level that the IPP is situated, can be calculated as in Equation 3.

$$\Psi = \cos^{-1} \left[\left(\frac{R_E}{R_E + h} \right) \cos E \right] - E \quad (3)$$

where E is the elevation angle of the radio source as seen from the LOFAR station. The direct distance along the raypath from the LOFAR station to the IPP (k) can then be estimated, using a spherical Earth approximation, as shown in Equation 4.

$$L = \sqrt{R_E^2 + (R_E + h)^2 - 2R_E(R_E + h)\cos \Psi} \quad (4)$$

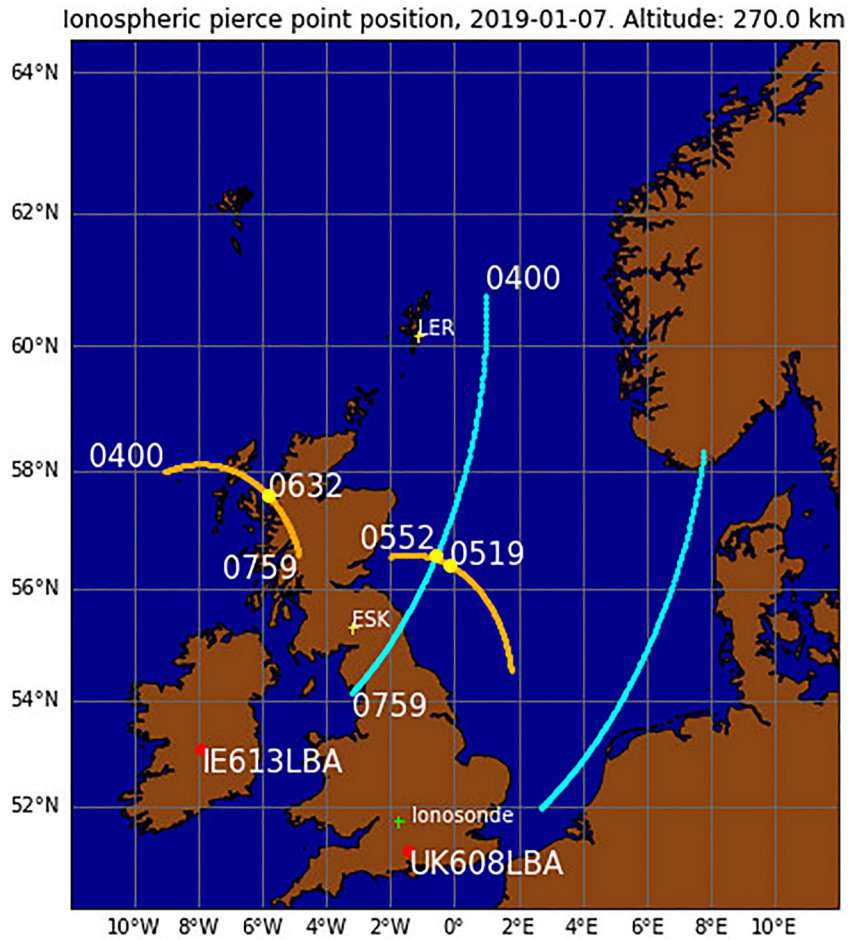


Figure 8. The positions of the ionospheric pierce point (IPP) for the Irish and UK LOW Frequency ARray (LOFAR) stations observing Cassiopeia A (orange arcs) and Cygnus A (blue arcs). The timings and positions of the IPP at the beginning and end of the observing window, and the various event onset times are shown. The positions of the LOFAR stations, ionosondes, and the Lerwick (LER) and Eskdalemuir (ESK) magnetometers are also given. Note the absence of an event onset time/position in the Cygnus A arc for the UK LOFAR station as the event was not seen in this observation.

Whilst it is not known exactly where in the raypath a given plasma feature is located, the altitude of the IPP can be assumed based on data, such as ionogram virtual heights. The angle Ψ is also useful in another respect in that it can be used, again assuming a spherical Earth approximation, to calculate the Great Circle distance from the LOFAR station to a point on the Earth's surface directly beneath the IPP, as shown in Equation 5.

$$d = 2\pi R_E(\Psi/2\pi) \quad (5)$$

Once d is obtained, and given that we know the geographic location of the LOFAR station, the corresponding longitude and latitude on the Earth's surface directly beneath the IPP can be approximated using the inverse Haversine function. For a given initial longitude (lon_0) and latitude (lat_0) at the location of the LOFAR station, and the azimuth of the radio source (Az), the position (lon_1 , lat_1) of the IPP can be calculated as in Equations 6 and 7.

$$\text{lat}_1 = \arcsin \left[\sin(\text{lat}_0) \times \cos\left(\frac{d}{R_E}\right) + \cos(\text{lat}_0) \times \sin\left(\frac{d}{R_E}\right) \times \cos(Az) \right] \quad (6)$$

$$\text{lon}_1 = \text{lon}_0 + \text{atan2} \left[\sin(Az) \times \sin\left(\frac{d}{R_E}\right) \times \cos(\text{lat}_1), \cos\left(\frac{d}{R_E}\right) - \sin(\text{lat}_0) \times \sin(\text{lat}_1) \right] \quad (7)$$

Given that the elevation and azimuth of the radio source is obtainable from its RA and Declination, we can now calculate the location of the IPP for any given time in the observing window. The accuracy of this approach

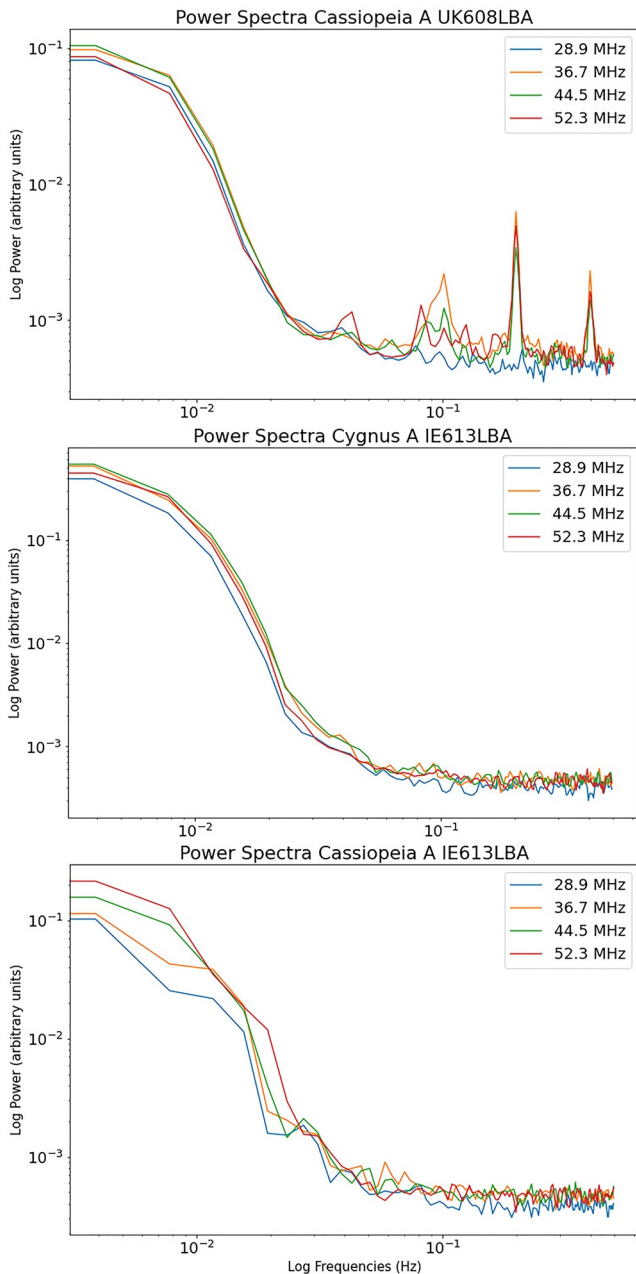


Figure 9. Power spectra for UK-CassA, Irl-CygA, and Irl-CassA at selected frequencies. The steepening of the spectra at 0.008 Hz is the Fresnel frequency.

can be refined further with geodesic models that more precisely represent the shape of the Earth b , for our purposes, the current method is sufficient. Figure 8 shows the calculated IPP for the UK and Irish LOFAR stations of both radio sources for an IPP altitude of 270 km, based on the average hmF2 obtained from the Fairford ionosonde. The orange and blue arcs are positions of the IPP for Cassiopeia A, and Cygnus A, respectively. The left hand pair of arcs are for the Irish LOFAR station, and the right hand pair are for the UK LOFAR station. The position and timing of event onsets in the various observations are also shown, as is the position of the LOFAR stations themselves, and other points of interest, such as the Fairford ionosonde, and ground based magnetometers at LER and ESK. The map is produced using the cartopy library routines in Python 3.

In Figure 8, for an assumed altitude of 270 km, the position of the IPP at event onset follows the time sequence of event onsets in the dynamic spectra (Figures 1 and 2). The feature is first seen, in any of the LOFAR data, at 0519 in UK-CassA. Onset is then seen at 0552 in Irl-CygA, and finally at 0632 in Irl-CassA. This would imply a TID propagating in an approximately West-North West direction, which is consistent with the GNSS TEC anomaly data shown in the previous section. The absence of activity in UK-CygA LOFAR data suggests the TID was quite localized and that for no plausible altitude does the UK-CygA arc lie far enough West to cross the position of the TID at any point.

3.4. TID Bulk Structure and Velocities

The large scale topology and bulk flow characteristics of the TID are clearly seen in the relative v TEC maps and ionosonde data. As can be seen from the dynamic spectra (Figures 1 and 2), the lead wavefront contains sub-structure at much finer scale sizes with lifetimes in the raypath of a few minutes. Four frequency channels corresponding to 28.9, 36.7, 44.5, and 52.3 MHz in each of UK-CassA, Irl-CygA, and Irl-CassA, were used to calculate the power spectral density covering the time occupied by the events seen in each observation, and each of these are shown in Figure 9.

In each case the power spectra show a fairly typical appearance for ionospheric scintillation, namely a flat plateau at the lowest frequencies which rapidly steepens (at the Fresnel frequency, f_F) and descends to the noise floor. The region of lowest frequencies below the f_F are from received signal power that has not yet fully formed a scintillation pattern during travel from the ionosphere to the observer. The region enclosed between the Fresnel frequency and the steep descent to the noise floor is signal power from fully formed ionospheric scintillation. The power spikes seen in UK-CassA are caused by residual RFI (they are notably absent from the 28.9 MHz channel). Strong cross-frequency coherence can be observed in these spectra, particularly in the UK-CassA and Irl-CygA observations, with the same Fresnel frequency being seen in each. Irl-CassA is slightly less coherent, consistent with the more prominent curvature of features seen in the dynamic spectra from this observation (Figure 3, bottom panel).

By combining the Fresnel frequency information from the power spectra with the calculated Fresnel scale sizes at the midpoints of each event observed, using Equations 1 and 4, we can estimate the plane-of-sky velocity of the plasma. The Fresnel scale, F_D , was calculated for the extrema of the bandwidth used by the LOFAR LBA, 25, and 65 MHz, and a middle frequency of 45 MHz. As the events recorded in the LOFAR data lasted for tens of minutes, the distance from the LOFAR station to the IPP at 270 km altitude, at the approximate midpoint of each event was used as the position of the event. The LOFAR-IPP distances (L) were calculated

Table 2
Fresnel Scale (F_D) and Corresponding Perpendicular Component of Plasma Drift Velocity, for the Midpoint of Each Observation

Freq. (MHz)/ λ (m)	F_D for UK-CassA (m)	F_D for Irl-CygA (m)	F_D for Irl-CassA (m)
25/12.0	4,002	3,889	3,769
45/6.7	2,983	2,899	2,809
65/4.6	2,482	2,412	2,338
L , F_D , and velocity	UK-CassA	Irl-CygA	Irl-CassA
L (km)	667	630	592
f_F (Hz)	0.008	0.008	0.008
v_p (ms^{-1}) for $\lambda = 12$ m	32	31	30
v_p (ms^{-1}) for $\lambda = 6.7$ m	24	23	22
v_p (ms^{-1}) for $\lambda = 4.6$ m	20	19	19
v_p (ms^{-1}) perp. to LOFAR raypath	25.3	24.3	23.7
SD (v_p)	6.2	5.0	4.6
Azimuth $- 90^\circ$	280.36	321.73	294.58
cos theta corrected velocity	62.2	55.4	63.6

Note. The Fresnel frequency, distances from the LOw Frequency ARray (LOFAR) station to the ionospheric pierce point (L) at the midpoint of the events seen in UK-CassA, Irl-CygA, and Irl-CassA, are also shown.

for UK-CassA, Irl-CygA, and Irl-CassA, as 667, 630, and 592 km respectively. Table 2 shows the Fresnel scale sizes for the stated frequencies at the distances quoted. Using Equation 2 we can calculate the component of ionospheric plasma drift velocity perpendicular to the LOFAR raypath (plane-of-sky), and these are also shown in Table 2.

As a further test of the consistency of these methods for finding the TID propagation velocity, the components of velocity perpendicular to the LOFAR raypaths are also shown in Table 2. These values can be multiplied by the cosine of the angle between the TID propagation velocity vector, as obtained from the vector averaging method, and the plane-of-sky velocity vector as seen from the LOFAR stations (at 90° to azimuth). As can be seen in Table 2, the results obtained by doing this in all three LOFAR observations are in very close agreement with the TID velocity obtained by vector averaging. It is notable that the velocity and propagation for similar events crossing the raypaths for the LOFAR core stations would be much better constrained given the large number of velocity vectors and power spectra that would be available. A further study investigating just such an event is currently ongoing.

By looking again at the TEC maps it is also possible to estimate the bulk velocity of the TID by noting how long it takes to move across the maps. Figure 10 shows TEC anomaly maps in time sequence starting at 0500 and stepping forward until 0655 (the approximate midpoint of the event seen in Irl-CassA). Also shown are the positions of the LOFAR IPPs at the midpoint of the respective events (red spots). Each pixel in these maps and in the Movies S1 is 0.5° in longitude and latitude which, at the surface of the Earth at mid latitude corresponds to a distance ~ 111 km. The TID takes approximately 30-minutes to cover a two pixel distance, so a simple distance over time estimate yields a velocity of $\sim 61 \text{ ms}^{-1}$, which is in very close agreement with the velocity calculated by the cos theta corrected velocities obtained using the power spectra. The full sequence of the TID propagation can be seen in the Movies S1 to this paper.

The first panel in Figure 10 shows the positions of the two wave peaks and the intervening trough of the TID at 0500. The first time it was seen in LOFAR was 0519 in UK-CassA; the IPP at the approximate midpoint of the event, at 0540, lies just beyond the lateral extent of the TID which is visible in GNSS data, as shown by the red dot. The blank areas are where no GNSS data was available to establish a TEC anomaly, but one can imagine the continuation of the lateral wavefront outwards to the Northeast and overlying the IPP at 0540. It is noticeable that by this time also the lead wave peak has, in the GNSS data at least, begun to break up, with the middle portion of the wave peak having disappeared. By the time of the midpoints of the later events, in Irl-CygA, and Irl-CassA respectively, the entire TID has become too incoherent to be seen in the GNSS TEC anomaly data. It

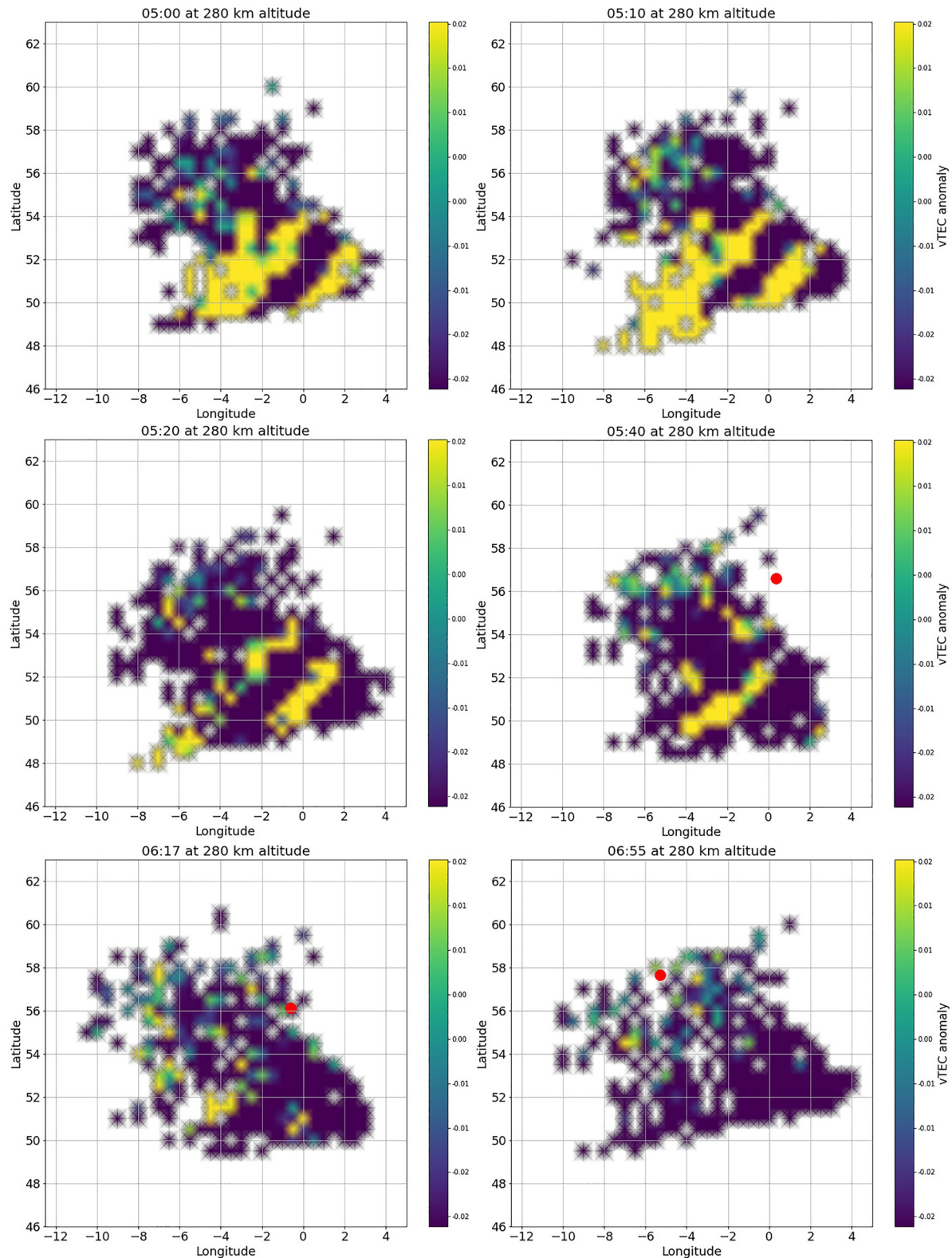


Figure 10. Global Navigation Satellite System Total Electron Content anomaly data, averaged to 30-min, showing the positions of the LOW Frequency ARray ionospheric pierce points (red spots) for the midpoints of the events in UK-CassA (0540), Irl-CygA (0617), and Irl-CassA (0655) respectively. The traveling ionospheric disturbance position at 0500–0520 with both wave peaks visible is also shown for context.

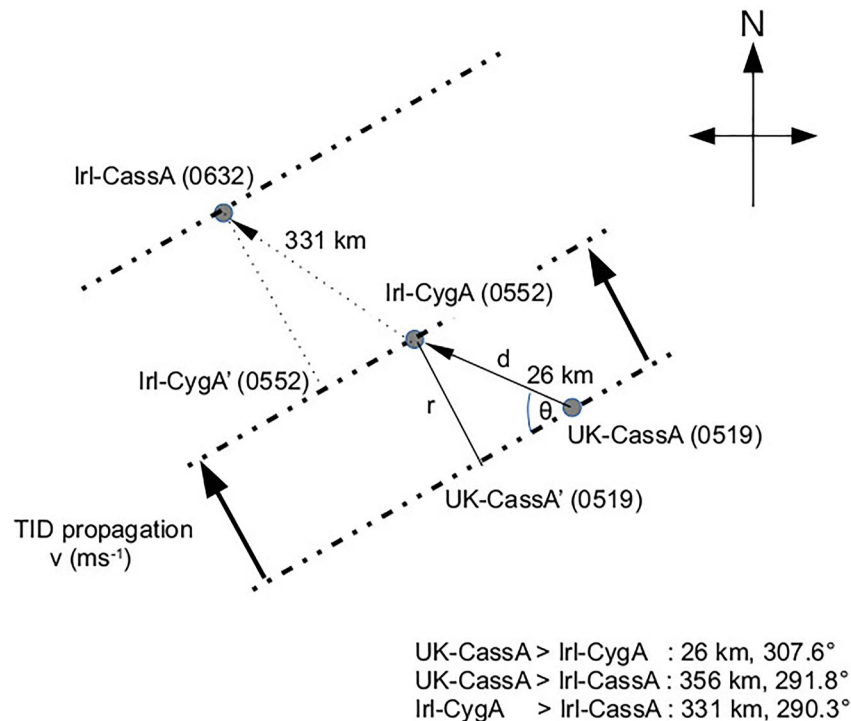


Figure 11. Modeled traveling ionospheric disturbance propagation using the velocity and bearings estimated from the Total Electron Content anomaly maps.

is evident that whilst the TID may no longer be coherent enough to appear in the GNSS data at these later times, it is certainly still present in the LOFAR data.

Understanding the motion of this particular TID was complicated by the fact that, as is apparent in the accompanying video, the direction of motion was not strictly perpendicular to the wavefront. As the TID moves Northwest it can be seen that the second wave peak gradually twists clockwise by a few degrees as it moves. Furthermore, the second wave peaks also appears to drift Westwards from approximately 0600 onwards. This Westward drift demonstrates that this complex movement is not merely a projection artifact, but a genuine separation and independent evolution of the two wave peaks which initially comprised the TID.

Given the estimated velocity and propagation bearing of the TID from the TEC anomaly maps of $\sim 60 \text{ ms}^{-1}$, and $\sim \text{NW}(315^\circ)$, respectively, we can use the timing of the TID in the LOFAR data and the positions of the various IPPs to provide a further estimate of these parameters. TID onset was first detected in UK-CassA at 0519, then in Irl-CygA at 0552, and finally in Irl-CassA at 0632. The onset times, great circle distances, and bearings between the IPPs are shown in Figure 11. The TID is modeled as a propagating plane wave, with the propagation direction perpendicular to the wavefront in an approximately NW direction. To avoid cluttering the diagram, the path between UK-CassA and Irl-CassA is not shown, however the distances and bearings for all IPP pairs are listed. The position UK-CassA' is the point on the TID wavefront which intersects the TID propagation axis at right angles and a line to the second IPP, as shown, likewise for Irl-CygA'.

The distance r in Figure 11 can be calculated simply by $r = d \sin(\theta)$, where θ is determined based on the assumed orientation of the TID plane wave, and d is the great circle distance between the first and second IPP. We can then use the distance r , and the velocity and propagation angle of the TID estimated from the TEC anomaly maps to predict when the TID should be visible in the second IPP. This technique relies on the assumption that the TID is a plane wavefront, and that the TID propagation velocity is constant between the IPPs.

Small scale structure within the TID preclude the accuracy of this technique over smaller distances. Given that UK-CassA and Irl-CygA lie only 26 km apart, the propagation between them is not estimated. However the distances between the other IPP pairs are larger, of the order of 300 km (see Figure 11). These calculations were made for a variety of TID propagation angles close to NW, with 335° yielding an expected TID

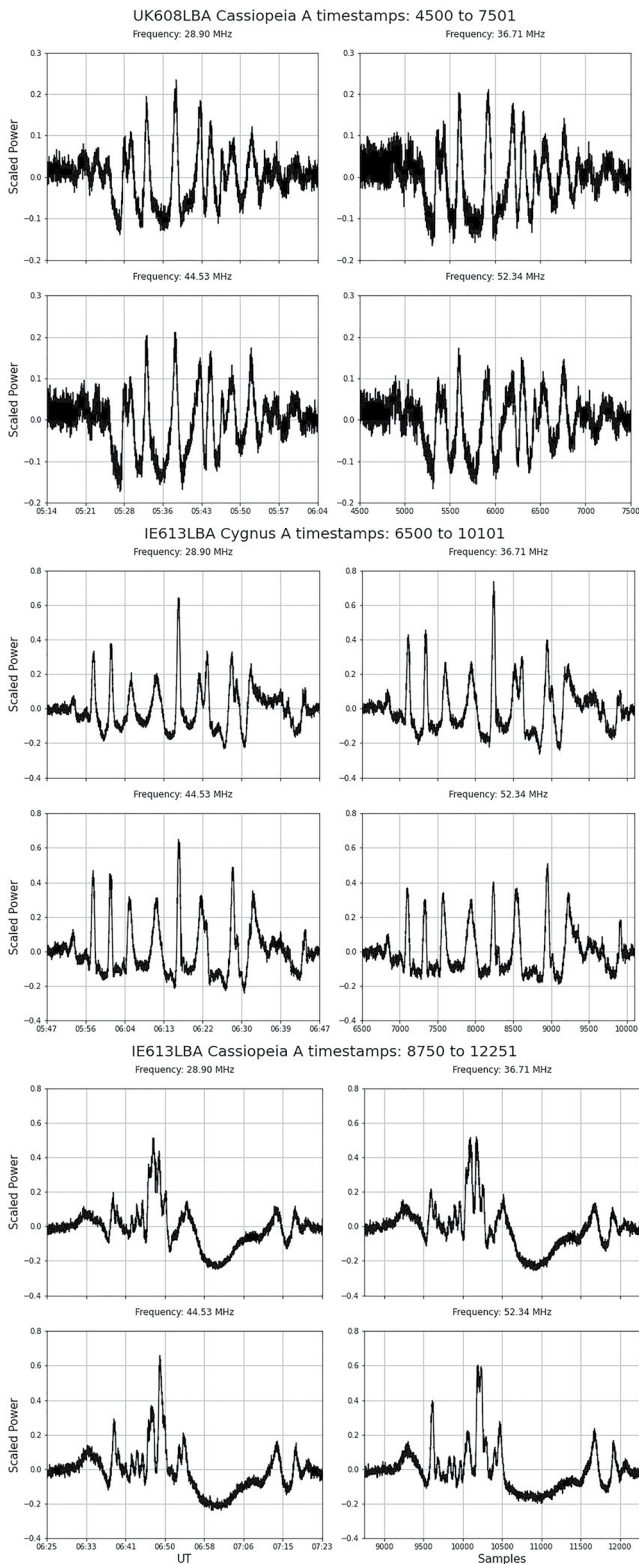


Figure 12. One dimensional time series of LOw Frequency ARray (LOFAR) data for each event at the frequencies shown.

visibility time in Irl-CassA of 0632 for the UK-CassA > Irl-CassA pair, and 0656 for the Irl-CygA > Irl-CassA pair. The 0632 expected visibility time for the UK-CassA > Irl-CassA pair is in very good agreement with the actual onset time of 0632. The expected visibility time of 0656 for the Irl-CygA > Irl-CassA pair is at the approximate mid-point of the TID visibility in Irl-CassA.

3.5. TID Substructure

Having acquired several estimates for the bulk velocity of the TID it is possible to investigate the properties of the finer substructure lying within the TID itself as revealed by the LOFAR data (Figure 3). Given the slow speed of the TID and the length of time these substructures spend in the raypath they are likely to be quite large. One dimensional time series from the four representative frequencies of 28.9, 36.7, 44.5, and 52.3 MHz, as used in Section 3.4, but windowed to the time around the events, are shown in Figure 12.

From these time series one can clearly see that the dominant modes of oscillation in all three events, across all frequencies, are lasting for several mines. In the data for Irl-CassA it can be seen that the TID has evolved significantly since it was seen earlier in Irl-CygA and UK-CassA, with a substantial signal fade lasting for approximately 20-mines. Further, the signal enhancements taper to noticeably sharper peaks than the signal fades which are broader; this is particularly noticeable in UK-CassA and Irl-CygA.

Figure 13 shows 2D periodograms generated using Welch's method, for all frequencies used in the LOFAR observations. These periodograms include one for UK-CygA even though no event was seen in that one, hence its featureless appearance. This was performed simply as a control test. The other periodograms all show lifetimes of larger plasma features crossing the raypath of the order of 300-s. Given a plasma drift velocity of $\sim 65 \text{ ms}^{-1}$, consistent with the velocity estimates in the previous section, the scale sizes of these features would be approximately 19.5 km. This is substantially larger than the Fresnel scale sizes calculated for the LOFAR wavelengths used here at LOFAR station-to-ionosphere distances of $\sim 650 \text{ km}$ (Table 2). Hence, the dominant plasma within the TID is are generating refractive scattering, with smaller structure contributing some ionospheric scintillation to the total received signal.

The near vertical features seen particularly in the periodograms for UK-CassA, and Irl-CygA, demonstrate that the scattering across the full observation bandwidth was largely non-dispersive. However by the time the TID crosses the raypath for Irl-CassA it has evolved significantly and begun to break up and dissipate (as seen in the TEC anomaly data). This evolution manifests in the 2D periodogram for Irl-CassA as multiple modes of oscillation at different observing frequencies.

4. Discussion and Summary

The ionosphere in these observations is essentially behaving as a large and rapidly deformable lens. Signal enhancement features in the LOFAR data (Figure 12) tend to be shorter lived than signal fades and they tend to bracket fades. Others have explored the concept of natural ionospheric lensing in the past, for example, Koval et al. (2017). More recently a model has been developed to investigate this concept with respect to LOFAR observations and the reader is referred to Boyde et al. (2022) for details.

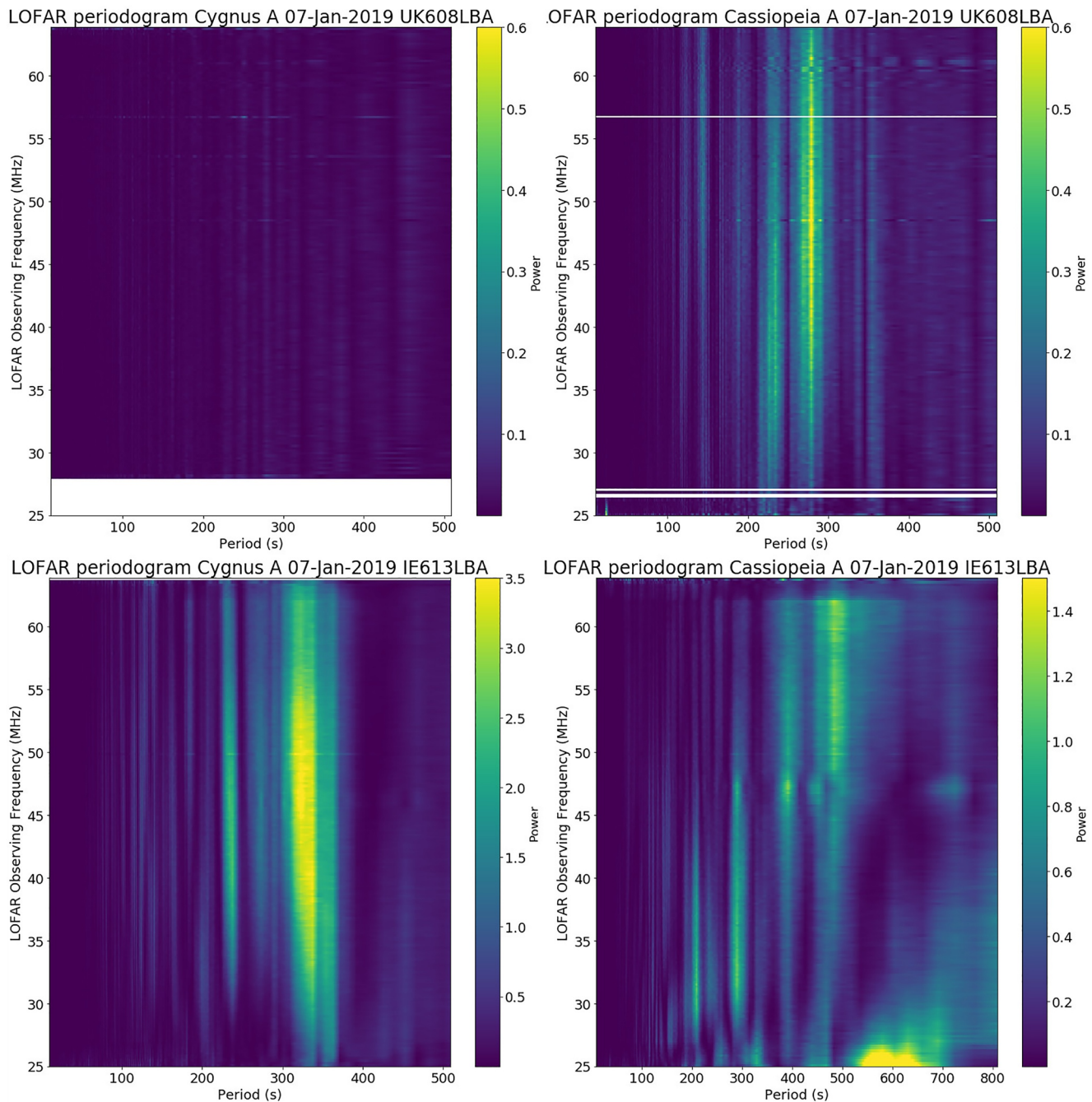


Figure 13. 2D periodograms generated using Welch's method, showing the dominant oscillation modes within the traveling ionospheric disturbance for UK and Irish Low Frequency ARray (LOFAR) stations on Cygnus A and Cassiopeia A across the full LOFAR observation bandwidth. The absence of any significant oscillations in the UK station observations for Cygnus A (top left) is consistent with the featureless dynamic spectrum for the same observation.

Fine structure signal enhancements can be exploited by radio astronomers by capturing the observing data at those points in time to produce, in principle, a higher resolution image of the target than would be possible if the ionosphere were not there. This is somewhat akin to the concept of lucky imaging in optical astronomy. Exploiting this effect across the entire LOFAR network would be very challenging given the localized scale sizes of the lensing features. However, given that each LOFAR station is in effect a radio telescope in its own right, this effect might still prove useful for radio astronomy observations from single stations. It may also be useful if exploited during observations from the LOFAR core, which contains many densely spaced individual LOFAR stations which would more likely all be under the same ionospheric fine structure if it is large enough.

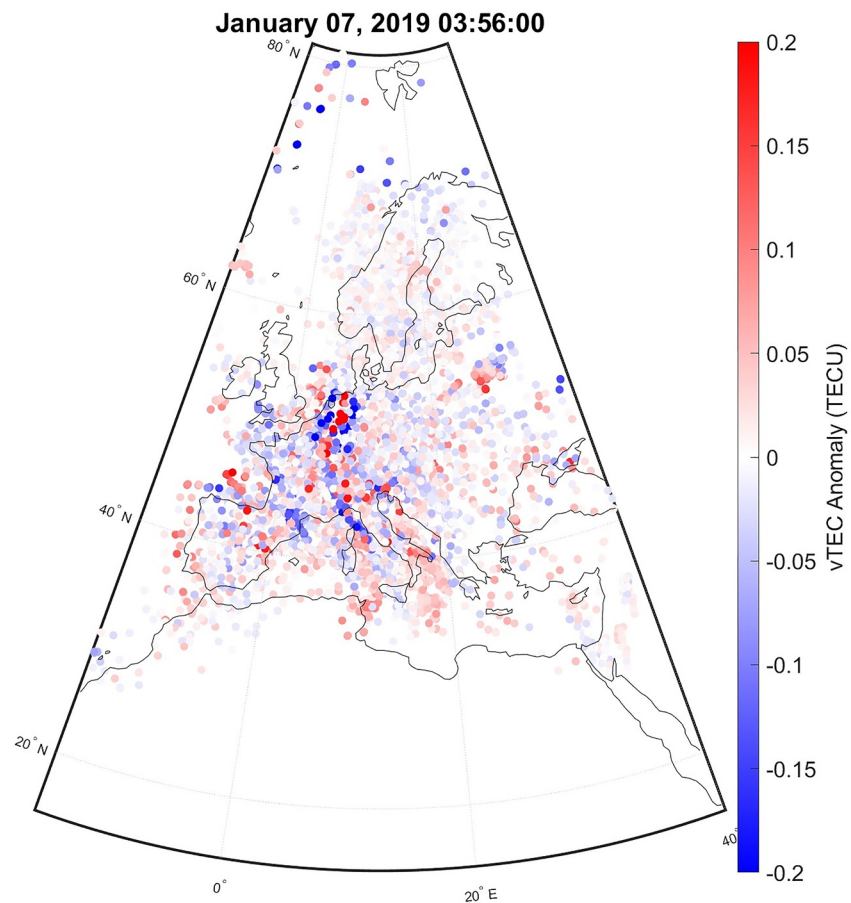


Figure 14. Larger arc-shaped traveling ionospheric disturbance structure drifting West across central Europe. The Northern arc of this structure drifts over the UK and is detected in the LOW Frequency ARray data.

Exploring substructure within TIDs has been attempted only a few times previously in the literature, such as by Alimov et al. (2008). These authors characterized the fractal nature of TIDs on spatial scales of $\sim 1\text{--}10$ km, quite closely matched to the size scales we have investigated here. Similarly, they made their observations at mid-latitude, under quiet geomagnetic conditions, by observing single frequency radio signals from orbital satellites at 150 MHz. TIDs typically have wavelengths extending sometimes for hundreds of km. However, results such as the present study, and Alimov et al. (2008), demonstrate that individual wave peaks within TIDs are themselves also comprised of wave trains on spatial scales smaller than the overall TID but larger than those which generate drifting ionospheric scintillation patterns from diffraction.

The TID observed in LOFAR appears to be related to a larger TID structure which was seen in TEC anomaly data to be drifting West across central Europe, as seen in Figure 14 and in the Europe-wide TEC anomaly video in Supporting Information S1 to this paper. This structure can be seen as a North-South oriented arc extending in latitude from Northern Italy to Denmark. The lead wave peak of the TID over the UK appears (see Figures 5 and 10) to break off from this larger feature and drift North West into the field-of-view of the UK and Irish LOFAR stations.

The bulk properties of the TID over the UK with a propagation velocity of ~ 60 ms^{-1} , a wavelength of order 100 km and a NW propagation axis are quite consistent with the bulk properties of night-time MSTID.

The authors considered the possibility that the overall structure was related to sunrise; Figure 15 shows the position of the solar terminator over Europe corrected for an altitude of 200 km at 0540, which is when the second of the two TID wave peaks over the UK lies above Southern England and the UK LOFAR station. As can be seen, the terminator for this altitude lies well to the East of the position of the second TID wave peak. Indeed sunrise at 200 km altitude does not occur at this position for approximately 1 hr after the second wave peak of

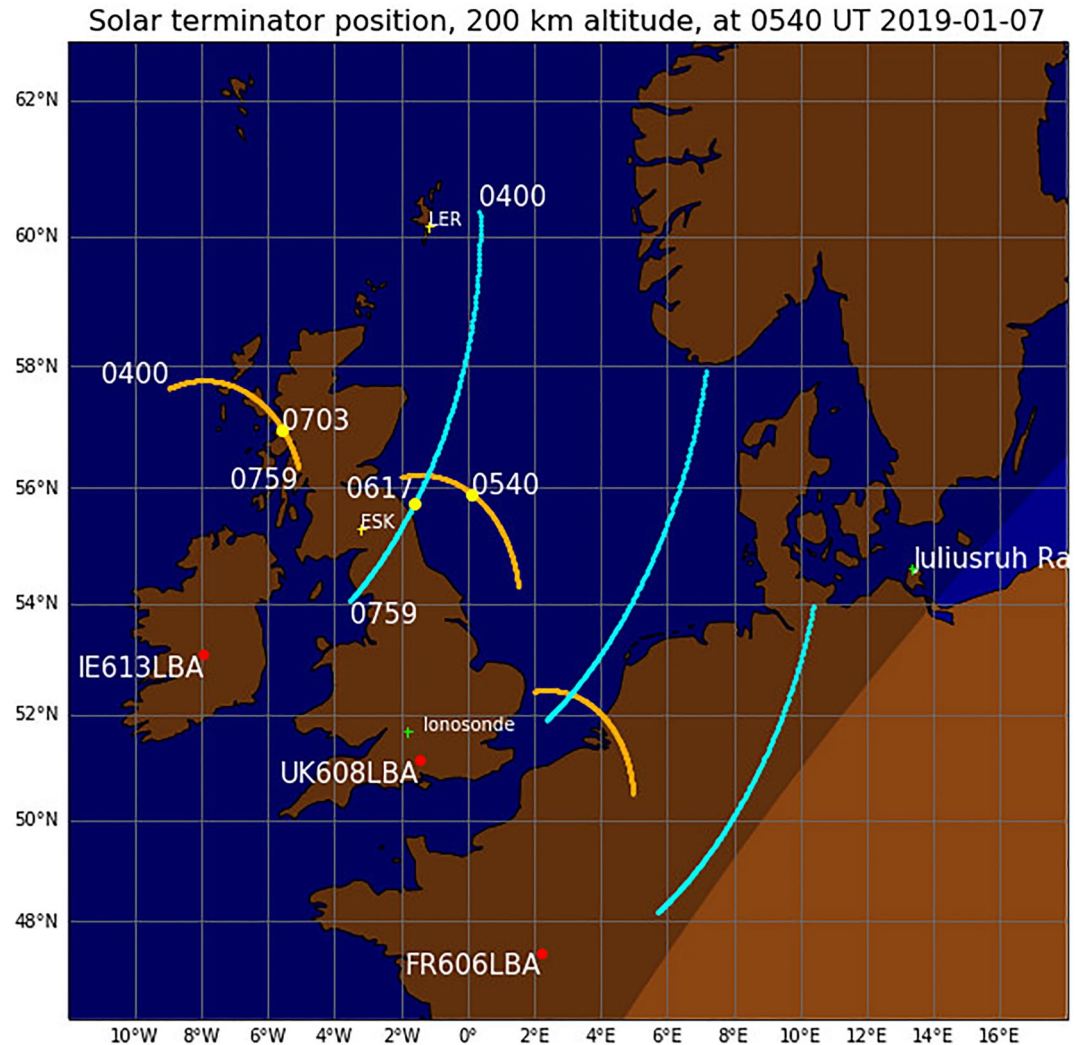


Figure 15. Solar terminator position, indicated by the light/dark shading boundary, corrected for an altitude of 200 km at 0540 when the second wave peak of the traveling ionospheric disturbance over the UK was passing over Southern England (Figures 5 and 10). The approximate midpoints for the events seen in Low Frequency ARray are also shown.

the TID has drifted out of the field-of-view of the UK GNSS TEC anomaly map. The TID is also not seen in any LOFAR stations to the East of the UK, including the LOFAR core.

Furthermore, the velocities of the solar terminator and the propagation speed of the TID are not well matched, with the TID propagation velocity being considerably slower than the velocity of the terminator. The relationship between the TID and the solar terminator is therefore ambiguous; further investigation of this is beyond the scope of the current paper.

Overall, these observations demonstrate the usefulness of LOFAR as an ionospheric observatory and offer the possibility to understand ionosphere behavior at previously unexplored time and frequency resolutions. The event described here was relatively simple and unambiguous; significantly more complex events are frequently encountered in the LOFAR archive, many showing highly-dispersive behavior, which will require more thorough analysis in future work, including developing an understanding of the relative importance of space weather versus terrestrial drivers of such phenomena.

5. Conclusions

We have investigated the characteristics of the propagation and fine substructure of a MSTID using wide bandwidth observations of trans ionospheric radio scattering with the LOFAR telescope. Further insights of the phenomena were obtained from ionosonde data and GNSS observations, which demonstrated its approximate altitude, global morphology, and evolution. The TID was observed dissipating in GNSS TEC anomaly maps, whilst still being visible in LOFAR observations as a result of the different observing sensitivities involved. LOFAR observations revealed the presence of refractive scattering from structures within the TID wave peak itself, with scale sizes of ~ 20 km, demonstrating LOFAR's utility as an ionospheric observatory.

Data Availability Statement

The LOFAR data used in this study are available from the LOFAR long-term archive: <https://lta.lofar.eu/>. The Kp- and Dst-indices are made available respectively by The Helmholtz Centre Potsdam—GFZ German Research Centre for Geosciences, and the World Data Centre for Geomagnetism, Kyoto. We thank the INTERMAGNET network, and ISGI (<https://isgi.unistra.fr>). The ACE solar wind data were sourced from the OMNI database at <http://omniweb.gsfc.nasa.gov>.

Acknowledgments

This paper is based on data obtained with the International LOFAR Telescope (ILT) under project code LT10_006. LOFAR (van Haarlem et al., 2013) is the LOFAR designed and constructed by ASTRON. It has observing, data processing, and data storage facilities in several countries, that are owned by various parties (each with their own funding sources), and that are collectively operated by the ILT foundation under a joint scientific policy. The ILT resources have benefited from the following recent major funding sources: CNRS-INSU, Observatoire de Paris and Université d'Orléans, France; BMBF, MIWF-NRW, MPG, Germany; Science Foundation Ireland (SFI), Department of Business, Enterprise and Innovation (DBEI), Ireland; NWO, The Netherlands; The Science and Technology Facilities Council, UK; Ministry of Science and Higher Education, Poland. RAF was partially supported by the LOFAR4SW project, funded by the European Community's Horizon 2020 Program H2020 INFRADEV-2017-1 under Grant 777442. The assistance of Chloe Ellerton with proof reading and technical checks is greatly appreciated. This work at the University of Birmingham is supported by a research grant from the Leverhulme Trust. The services of the Natural Environment Research Council (NERC) British Isles continuous GNSS Facility (BIGF), www.bigf.ac.uk, in providing archived GNSS data to this study, are gratefully acknowledged. B. Dabrowski and A. Krankowski thank the National Science Centre, Poland for granting "LOFAR observations of the solar corona during Parker Solar Probe perihelion passages" in Beethoven Classic 3 funding initiative under project number 2018/31/G/ST9/01341. The UWM authors also thank the Ministry of Education and Science (MES), Poland for granting funds for the Polish contribution to the International LOFAR Telescope (Agreement 2021/WK/02).

References

- Aarons, J. (1982). Global morphology of ionospheric scintillations. *Proceedings of the IEEE*, 70(4), 360–378. <https://doi.org/10.1109/PROC.1982.12314>
- Abdu, M. A., Batista, I. S., Sobral, J. H. A., de Paula, E. R., & Kantor, I. J. (1985). Equatorial ionospheric plasma bubble irregularity occurrence and zonal velocity under quiet and disturbed conditions from Polarimeter observations. *Journal of Geophysical Research*, 90(A10), 9921–9928. <https://doi.org/10.1029/JA090iA10p09921>
- Alimov, V. A., Vybornov, F. I., & Rakhlin, A. V. (2008). On the fractal structure of small-scale travelling ionospheric disturbances. *Radiophysics and Quantum Electronics*, 51(1), 20–27. <https://doi.org/10.1007/s11141-008-9001-2>
- Basu, S., Weber, E., Bullett, T., Keskinen, M., MacKenzie, E., Doherty, P., et al. (1998). Characteristics of plasma structuring in the cusp/cleft region at Svalbard. *Radio Science*, 33(6), 1885–1899. <https://doi.org/10.1029/98RS01597>
- Birch, M. J., Hargreaves, J. K., & Bailey, G. J. (2002). On the use of an effective ionospheric height in electron content measurement by GPS reception. *Radio Science*, 37(1), 15–1–15–19. <https://doi.org/10.1029/2000RS002601>
- Booker, H. G. (1981). Application of refractive scintillation theory to radio transmission through the ionosphere and the solar wind, and to reflection from a rough ocean. *Journal of Atmospheric and Terrestrial Physics*, 43(11), 1215–1233. [https://doi.org/10.1016/0021-9169\(81\)90036-2](https://doi.org/10.1016/0021-9169(81)90036-2)
- Booker, H. G., & Majidihi, G. (1981). Theory of refractive scattering in scintillation phenomena. *Journal of Atmospheric and Terrestrial Physics*, 43(11), 1199–1214. [https://doi.org/10.1016/0021-9169\(81\)90035-0](https://doi.org/10.1016/0021-9169(81)90035-0)
- Bowman, G. G. (1981). The nature of ionospheric spread-F irregularities in mid-latitude regions. *Journal of Atmospheric and Terrestrial Physics*, 43(1), 65–79. [https://doi.org/10.1016/0021-9169\(81\)90010-6](https://doi.org/10.1016/0021-9169(81)90010-6)
- Boyde, B., Wood, A., Dorrian, G., Fallows, R. A., Themens, D., Mielich, J., et al. (2022). Lensing from small-scale travelling ionospheric disturbances observed using LOFAR. *Journal of Space Weather and Space Climate*, 12, 34. <https://doi.org/10.1051/swsc/2022030>
- Carrano, C. S., Groves, K. M., Caton, R. G., Rino, C. L., & Straus, P. R. (2011). Multiple phase screen modelling of ionospheric scintillation along radio occultation raypaths. *Radio Science*, 46(6), RS0D07. <https://doi.org/10.1029/2010RS004591>
- Cervera, M. A., & Harris, T. J. (2014). Modelling ionospheric disturbance features in quasi vertically incident ionograms using 3-D magnetoionic ray tracing and atmospheric gravity waves. *Journal of Geophysical Research: Space Physics*, 119(1), 431–440. <https://doi.org/10.1002/2013JA019247>
- Cherniak, I., & Zakharenkova, I. (2018). Large-scale travelling ionospheric disturbances origin and propagation: Case study of the December 2015 geomagnetic storm. *Space Weather*, 16(9), 1377–1395. <https://doi.org/10.1029/2018SW001869>
- de Gasperin, F., Mevius, M., Rafferty, D. A., Intema, H. T., & Fallows, R. A. (2018). The effect of the ionosphere on ultra-low-frequency radio-interferometric observations. *Astronomy and Astrophysics*, 615, A179. <https://doi.org/10.1051/0004-6361/201833012>
- Fallows, R. A., Coles, W. A., McKay-Bukowski, D., Vierinen, J., Virtanen, I. I., Postila, M., et al. (2014). Broadband meter-wavelength observations of ionospheric scintillation. *Journal of Geophysical Research: Space Physics*, 119(12), 10544–10560. <https://doi.org/10.1002/2014JA020406>
- Fallows, R. A., Forte, B., Astin, I., Allbrook, T., Arnold, A., Wood, A., et al. (2020). A LOFAR observation of ionospheric scintillation from two simultaneous travelling ionospheric disturbances. *Journal of Space Weather and Space Climate*, 10, 10. <https://doi.org/10.1051/swsc/2020010>
- Fejer, B. G., & Kelley, M. C. (1980). Ionospheric irregularities. *Reviews of Geophysics and Space Physics*, 18(2), 401–405. <https://doi.org/10.1029/rg018i002p0401>
- Forte, B. (2008). Refractive scattering evidence from multifrequency scintillation spectra observed at auroral latitudes. *Radio Science*, 43(2), RS2012. <https://doi.org/10.1029/2007RS003715>
- Fremouw, E. J., & Bates, H. F. (1971). Worldwide behaviour of average VHF/UHF scintillation. *Radio Science*, 6(10), 863–869. <https://doi.org/10.1029/rs006i010p00863>
- Greenwald, R. A., Baker, K. B., Dudeney, J. R., Pinnock, M., Jones, T. B., Thomas, E. C., et al. (1995). DARN/SuperDARN. *Space Science Reviews*, 71(1–4), 761–796. <https://doi.org/10.1007/BF00751350>
- Groves, K. M., Basu, S., Weber, E. J., Smitham, M., Kuenzler, H., Valladares, C. E., et al. (1997). Equatorial scintillation and systems support. *Radio Science*, 32(5), 2047–2064. <https://doi.org/10.1029/97RS00836>
- Hinder, R., & Ryle, M. (1971). Atmospheric limitations to the angular resolution of aperture synthesis radio telescopes. *MNRAS*, 154(2), 229–253. <https://doi.org/10.1093/mnras/154.2.229>

- Hines, C. O. (1960). Internal atmospheric gravity waves at ionospheric heights. *Canadian Journal of Physics*, 38(11), 1441–1481. <https://doi.org/10.1139/p60-150>
- Hunsucker, R. D. (1982). Atmospheric gravity waves generated in the high-latitude ionosphere: A review. *Reviews of Geophysics*, 20(2), 293–315. <https://doi.org/10.1029/RG020i002p00293>
- Kinrade, J., Mitchell, C. N., Yin, P., Smith, N., Jarvis, M. J., Maxfield, D. J., et al. (2012). Ionospheric scintillation over Antarctica during the storm of 5–6 April 2010. *Journal of Geophysical Research*, 117(A5), A05304. <https://doi.org/10.1029/2011JA017073>
- Kintner, P. M., Ledvina, B. M., & de Paula, E. R. (2007). GPS and ionospheric scintillations. *Space Weather*, 5(9), S09003. <https://doi.org/10.1029/2006SW000260>
- Koval, A., Chen, Y., Stanislavsky, A., & Zhang, Q. H. (2017). Travelling ionospheric disturbances as huge natural lenses: Solar radio emission focusing effect. *Journal of Geophysical Research: Space Physics*, 122(9), 9092–9101. <https://doi.org/10.1002/2017JA024080>
- Mangum, J. G., & Wallace, P. (2015). Atmospheric refractive electromagnetic wave bending and propagation delay. *Publications of the Astronomical Society of the Pacific*, 127, 947–991. <https://doi.org/10.1086/679582>
- Mitchell, C. N., Alfonsi, L., De Franceschi, G., Lester, M., Romano, V., & Wernik, A. W. (2005). GPS TEC and scintillation measurements from the polar ionosphere during the October 2003 storm. *Geophysical Research Letters*, 32(12), L12S03. <https://doi.org/10.1029/2004GL021644>
- Moskaleva, E. V., & Zaalov, N. Y. (2013). Signature of polar cap inhomogeneities in vertical sounding data. *Radio Science*, 48(5), 547–563. <https://doi.org/10.1002/rds.20060>
- Muralikrishna, P., Vieira, L. P., & Abdu, M. A. (2007). Spectral features of E- and F-region plasma irregularities as observed by rocket-borne electron density probes from Brazil. *Revista Brasileira de Geofísica*, 25(2), 115–128. <https://doi.org/10.1590/s0102-261x2007000600014>
- Nishitani, N., Ruohoniemi, J. M., Lester, M., Baker, J. B. H., Koustov, A. V., Shepherd, S. G., et al. (2019). Review of the accomplishments of mid-latitude Super Dual Auroral Radar Network (SuperDARN) HF radars. *Progress in Earth and Planetary Science*, 6(1), 27. <https://doi.org/10.1186/s40645-019-0270-5>
- Prikryl, P., Jayachandran, P. T., Chadwick, R., & Kelly, T. D. (2015). Climatology of GPS phase scintillation at northern high latitudes for the period 2008 to 2013. *Annales Geophysicae*, 33(5), 531–545. <https://doi.org/10.5194/angeo-33-531-2015>
- Priyadarshi, S. (2015). A review of ionospheric scintillation models. *Surveys in Geophysics*, 36(2), 295–324. <https://doi.org/10.1007/s10712-015-9319-1>
- RamaRao, P. V. S., TulasiRam, S., Gopi Krishna, S., Niranjana, K., & Prasad, D. S. V. V. D. (2006). Morphological and spectral characteristics of L-band and VHF scintillations and their impact on trans-ionospheric communications. *Earth Planet Space Science*, 58(7), 895–904. <https://doi.org/10.1186/bf03351994>
- Reinisch, B. W., & Galkin, I. A. (2011). Global ionospheric radio observatory (GIRO). *Earth Planets and Space*, 63(4), 377–381. <https://doi.org/10.5047/eps.2011.03.001>
- Shiokawa, K., Ihara, C., Otsuka, Y., & Ogawa, T. (2003). Statistical study of nighttime medium-scale travelling ionospheric disturbances using midlatitude airglow images. *Journal of Geophysical Research*, 108, 1052. <https://doi.org/10.1029/2002JA009491>
- Singleton, D. G. (1970). Saturation and focusing effects in radio-star and satellite scintillations. *Journal of Atmospheric and Terrestrial Physics*, 32(2), 187–208. [https://doi.org/10.1016/0021-9169\(70\)90191-1](https://doi.org/10.1016/0021-9169(70)90191-1)
- Song, K., Meziane, K., Kashcheyev, A., & Jayachandran, P. T. (2022). Multifrequency observation of high latitude scintillation: A comparison with the phase screen model. *IEEE Transactions on Geoscience and Remote Sensing*, 60, 1–9. <https://doi.org/10.1109/TGRS.2021.3113778>
- Themens, D. R., Watson, C., Žagar, N., Vasylyevych, S., Elvidge, S., McCaffrey, A., et al. (2022). Global propagation of ionospheric disturbances associated with the 2022 Tonga volcanic eruption. *Geophysical Research Letters*, 49(7), e2022GL098158. <https://doi.org/10.1029/2022GL098158>
- Tsunoda, R. T. (1985). Control of the seasonal and longitudinal occurrence of equatorial scintillations by the longitudinal gradient in integrated E region Pedersen conductivity. *Journal of Geophysical Research*, 90(A1), 447–456. <https://doi.org/10.1029/JA090iA01p00447>
- Tsunoda, R. T. (1988). High latitude F-region irregularities: A review and synthesis. *Reviews of Geophysics*, 26(4), 719–760. <https://doi.org/10.1029/rg026i004p00719>
- van Haarlem, M. P., Wise, M. W., Gunst, A. W., Heald, G., McKean, J. P., Hessels, J. W. T., et al. (2013). LOFAR: Low-frequency-array. *Astronomy and Astrophysics*, 556, A2. <https://doi.org/10.1051/0004-6361/201220873>
- Wild, J. P., & Roberts, J. A. (1956). The spectrum of radio-star scintillations and the nature of irregularities in the ionosphere. *Journal of Atmospheric and Terrestrial Physics*, 8(1–2), 55–75. [https://doi.org/10.1016/0021-9169\(56\)90091-5](https://doi.org/10.1016/0021-9169(56)90091-5)
- Yeh, K. C., & Liu, C.-H. (1982). Radio wave scintillations in the ionosphere. *Proceedings of the IEEE*, 70(4), 324–360. <https://doi.org/10.1109/proc.1982.12313>